Evaluation of correlated Pandora column NO_2 and *in situ* surface NO_2 measurements during GMAP campaign

Lim-Seok Chang[1], Donghee Kim[1], Hyunkee Hong[1], Deok-Rae Kim[1], Jeonga Yu[1],

Kwangyul Lee[1], Hanlim Lee[2], Daewon Kim[2], Jinkyu Hong[3], Hyun-Young Jo[4],

and Cheol-Hee Kim[4, 5]

[1] *Environmental Satellite Center, National Institute of Environmental Research, Incheon, 22689, Republic of Korea*

[2] *Department of Spatial Information Engineering, Pukyong National University, Busan, 48547, Republic of Korea*

[3] *Department of Atmospheric Sciences, Yonsei University, Seoul, 03722, Republic of Korea*

[4] *Institute of Environmental Studies, Pusan National University, Busan, 46241, Republic of Korea*

[5] *Department of Atmospheric Sciences, Pusan National University, Busan, 46241, Republic of Korea*

Correspondence:

Cheol-Hee Kim (chkim2@pusan.ac.kr), and Lim-Seok Chang (lschang@korea.kr)

Abstract.

To validate the Geostationary Environment Monitoring Spectrometer (GEMS), the GEMS Map of Air Pollution (GMAP) campaign was conducted during 2020–2021 by integrating Pandora Asia Network, aircraft, and *in situ* measurements. In the present study, GMAP-2020 measurements were applied to evaluate urban air quality and explore the synergy of Pandora column (PC) NO_2 measurements and surface *in situ* (SI) NO_2 measurements for Seosan, South Korea, where large point source (LPS) emissions are densely clustered. Due to the difficulty of interpreting the effects of LPS emissions on air quality downwind of Seosan using SI monitoring networks alone, we explored the combined analysis of both PC-NO_2 and SI-NO_2 measurements. Agglomerative hierarchical clustering using vertical meteorological variables combined with PC-NO_2 and SI-NO_2 yielded three distinct conditions: synoptic wind-dominant (SD), mixed (MD), and local wind-dominant (LD). These results suggest meteorology-dependent correlations between PC-NO_2 and SI-NO_2. Overall, yearly daytime mean (11:00–17:00 KST) PC-NO_2 and SI-NO_2 statistical data showed good linear correlations (R = ~0.73); however, the differences in correlations were largely attributed to meteorological conditions. SD conditions characterized by higher wind speeds and advected marine boundary layer heights suppressed fluctuations in both PC-NO_2 and SI-NO_2, driving a uniform vertical NO_2 structure with higher correlations, whereas under LD conditions, LPS plumes were decoupled from the surface or were transported from nearby cities, weakening correlations through anomalous vertical NO_2 gradients. The discrepancies suggest that using either PC-NO_2 or SI-NO_2 observations alone involves a higher possibility of uncertainty under LD conditions or prevailing transport processes. However, under MD conditions, both pollution ventilation due to high surface wind speeds and daytime photochemical NO_2 loss contributed to stronger correlations through a decline in both PC-NO_2 and SI-NO_2 toward noon. Thus, Pandora Asia Network observations collected over 13 Asian countries since 2021 can be utilized for detailed investigation of the vertical complexity of air quality, and the conclusions can be also applied when performing GEMS observation interpretation in combination with SI measurements.

1. Introduction

Rapid developments in environmental remote sensing have led to a new era of air quality observations, and recent hyperspectral data retrieval technologies have allowed for routine and accurate monitoring of air pollutants at high spatial and temporal resolution. In particular, the Geostationary Environment Monitoring Spectrometer (GEMS), which was launched on February 18, 2020, measures the total and tropospheric air pollutant columns hourly at spatial resolutions of 7 km × 8 km for gas and 3.5 km × 8 km for aerosols (Kim et al., 2020), facilitating the tracking of pollution transport from local to synoptic scales.

Recent studies have revealed the potential of satellite observations to evaluate surface air quality, particularly in regions with sparse air quality-monitoring networks. The main approach is to convert column density to surface concentrations using a shape factor of the ratio of the partial column (Ω_{z_0}) within the lowest layer (z_0) to the total column (Ω_{total}) (Zhao *et al.*, 2019), as follows:

$$\mathrm{S} = \frac{\Omega_{z_0}}{\Omega_{\mathrm{total}}} \times \frac{C}{\Delta z_o} \ ,$$

where S, C, and Δz_o are the surface concentration, column density, and lowest layer thickness, respectively. Acquiring accurate profile shape information is critical for determining the relationship between the column amount and surface concentration because the shape factor is spatiotemporally variable. Considering this, numerous studies have obtained close relationships using chemical transport model simulations, aircraft *in situ* measurements, and satellite observations with high correlation coefficients (R) of 0.7 or more and used them to scale up surface NO_2 to column NO_2 (Wang and Christopher, 2003; Boersma *et al.*, 2009; Lamsal *et al.*, 2010). This strong correlation can be explained by the generally uniform planetary boundary layer height (PBLH), and by aerosol type and abundance, which is also the case for trace gases.

By contrast, the implications of weak correlations between column and surface measurements remain unclear. Engel-Cox *et al.* (2004) found a negative correlation of AOD and surface $PM_{2.5}$ in northwestern USA, and explained it based on elevated haze decoupled from the surface. Thompson *et al.* (2019) examined weak correlations between Pandora column (PC) measurements and surface *in situ* (SI) observations of NO_2 over the Yellow Sea during the Korea–US air quality (KORUS-AQ) field study, and suggested, as a possible reason, the transported non-uniform plumes originated in China and Seoul hundreds of meters above the ground from the surface layer. The estimated surface $PM_{2.5}$ concentration was weakly correlated (R = 0.4–0.49) with observed $PM_{2.5}$ concentrations in Seoul, because only PBLH was added to the multi-linear regression model to correlate AOD to surface $PM_{2.5}$ (Kim *et al.*, 2021). This effect may be related to the significant impact of long-range transport on $PM_{2.5}$, with a contribution of up to 39% in Seoul (Lee *et al.*, 2021). Thus, the wide variability in the degree of correlation between PC-PM and SI-PM is closely related to vertical profile variability (Flynn *et al.*, 2016).

It appears highly probable that several factors are responsible for the correlations between PC-NO_2 and SI-NO_2; therefore, it is necessary to improve our understanding of the degree of correlation through detailed measurements, including column concentration. In this study, we focused on the impact of meteorology and chemistry on correlation variability using PC, SI and aircraft measurements, as well as meteorological observations. Understanding vertical profile variability is also useful for evaluating the effects of various emissions on urban air quality, particularly in areas neighboring active large point source (LPS) emissions sites. Quantifying the impact of LPS emissions on downwind cities remains challenging due to the lack of three-dimensional (3D) measurements. Accurate vertical profile data are also useful for improving remote sensing retrieval algorithms, because the profile shape contributes to the conversion of slant column density into vertical column density as part of the air mass factor. In mid-2019, the Pandonia Global Network (PGN; https://pandonia-global-network.org) was launched, with support from the National Aeronautics and Space Administration (NASA) and European Space Agency (ESA), to facilitate the validation and verification of low-orbit or geostationary environmental satellites. This network is attempting to expand air quality monitoring through integration with existing long-term air quality monitoring stations. Since 2020, the National Institute of Environmental Research, Economic and Social Commission for Asia and the Pacific, and Korea Environment Corporation have been extending the Pandora Asia Network to include 13 Asian countries, with support from the Korea International Cooperation Agency. The Pandora Asia Network is expected to be widely used to study urban air quality in Asia, which is increasingly deteriorating due to rapid economic growth.

As part of the GEMS Map of Air Pollution (GMAP) campaign, a suite of Pandora instruments was deployed in Seosan, a South Korean coastal city, from November 2020 to January 2021 (GMAP-2020), and we applied GMAP-2020 measurements to explore the synergy of PC observations when evaluating air quality over Seosan. Further results from this research project are also reported in this special issue, including GEMS validation and urban air quality evaluations based on Pandora, aircraft, surface flux, and *in situ* surface chemical measurements conducted during GMAP-2020.

2. GMAP-2020 campaign

GEMS was launched on February 19, 2020; it is the first instrument to observe air quality from a geostationary Earth orbit. GEMS provides hourly air quality data on aerosols and gases at a spatial resolution of 7 km × 8 km. It is a scanning ultraviolet (UV)-visible spectrometer that observes key atmospheric constituents including O_3, NO_2, CO, SO_2, CH_2O, CHOCHO, aerosols, clouds, and UV indices. This mission heralded a new era of satellite air quality monitoring and will be joined by NASA's Tropospheric Emissions: Monitoring of Pollution (TEMPO) and ESA's Sentinel-4 to form the GEO Air Quality Constellation in ~3 years, to cover the most polluted region in the Northern Hemisphere.

During GMAP-2020, Pandora instruments (PA_1–PA_4) were deployed near large point sources (LPS_1–LPS_4) in Seosan; *in situ* surface air quality monitoring systems (AQM_1–AQM_6) and meteorological observations (Met_1–Met_3) were also used in this study (see their locations in Fig. 1). Aircraft measurements were also used to validate GEMS and diagnose LPSs located in industrial areas surrounding Seosan. We explored the synergy of Pandora observations and SI measurements, based on measurements collected during GMAP-2020, by evaluating air quality in industrial Seosan (where LPSs are densely clustered). We particularly investigated the impacts of vertical profile and sub-pixel variability for trace gases and aerosols, for further GEMS validation. All measurement sites for both GMAP-2020 campaigns are indicated in Figure 1.

3. Methods

3.1 Study area

Seosan, the target area of the GMAP-2020 campaign, is a small city with a population of 174,780 in 2017; it is accessed via three expressways to the east and four national highways cross the city. It is located in midwestern South Korea, and is affected by >300 emissions point sources including LPSs. Coal-fired power plants including Taean, Dangjin, the Hyundai Dangjin steelworks, and the Daesan petrochemistry industrial complex (LPS_1–LPS_4, respectively, in Fig. 1) have the highest emissions rates in South Korea. The Hyundai Dangjin steelworks (LPS_3) and Taean and Dangjin power plants (LPS_1 and LPS_2) emit 10.5, 11, and 8.8 Gg of NOx per year, respectively. Although Seosan accounts for only 1.8% of the population of Seoul, its NOx emissions (10.2 Gg $year^{-1}$) account for 13.2% of its total NOx emissions. The transportation sector of Seosan is a far greater NOx source than the industrial sector of Seoul (ratio of 99:1); however, within Seosan, the industrial sector is on par with the transport sector (52:48; http://airemiss.nier.go.kr).

During the past decade, the annual mean NO_2 level in Seosan has been 17 ppb, which is approximately half of that in Seoul (31.2 ppb). NO_2 exhibits strong seasonal variation, reaching a minimum in summer and maximum in winter, due to meteorological factors and greater energy use during winter (Kim and Kim, 2020). Therefore, the timing of the GMAP-2020 campaign was well suited to tracking pollution.

3.2 Pandora measurements

Pandora measures the UV and visible wavelengths (280–525 nm) of direct sunlight with a spectral resolution of 0.6 nm, to determine the vertical column density of NO_2, O_3, and HCHO (Herman *et al.*, 2009). For measurements in Dobson units (DU; 1 DU = 26.9 Pmol cm^{-2}), column NO_2 has a very high signal-to-noise ratio (700:1) and very high precision (0.01 DU) for clear skies (Herman *et al.*, 2009). The vertical column density of NO_2 can be determined using DOAS software (Van Roozendael and Fayt, 2001). Pandora direct-sun measurements are advantageous in that the air mass factor is simplified, and therefore is dependent only on the geography for a known solar zenith angle.

Four Pandora instruments were installed at sites to the south of LPSs (Fig. 1) during the GMAP-2020 campaign, i.e., at Seosan Daehoji, Seosan Dongmun, Seosan City Council, and Seosan Super Site (PA_1–PA_4 in Fig. 1). The presence of clouds reduces vertical column density precision by decreasing the number of photons arriving at Pandora instruments within a fixed integration time. Therefore, the retrieved Pandora measurements were cloud-screened using an observed cloud cover of 0.6. Cloud cover was provided by the Korea Meteorological Administration (KMA), and the precision improvement afforded by cloud screening was verified by comparing each Pandora-derived vertical column density with the median vertical column density, with and without cloud screening within the inter-comparison period.

At PA_4, the operating period was extended to cover almost the entire year (November 12, 2020–October 30, 2021) including the GMAP-2020 campaign period, and the Pandora spectra were processed into vertical column density data for trace gases using the standard NO_2 algorithm in BlickP software provided by PGN (Cede, 2019). The resultant PC-NO_2 data were obtained from the PGN website (https://pandonia-global-network.org) for the 1-year period from Nov. 12, 2020 to Oct. 30, 2021, and were also used as PC-NO_2 statistics for PA_4, in this study.

3.3 Surface and airborne chemical measurements

Hourly average data for SI-NO_2 over a period of 1 year were obtained from Ministry of Environment AQM network stations in Seosan: Pandori, Leewon, Taean, Dongmoon, Seongyeon, and Daesan (AQM_1–AQM_6, respectively, in Fig. 1). The Seosan Super Site (PA_4/AQM_1) provided hourly data for NO and NOy via an NO-DIF-NOy analyzer (42i-Y; Thermo Scientific, Waltham, MA, USA), and for $PM_{2.5}$ chemical species using an ambient ion monitor (AIM; URG 9000D, URG Corp., Chapel Hill, NC, USA). Weekly zero and span checks were conducted for NOy calibration, to ensure that differences between checks remained <3%. Water-soluble ions in aerosol and gaseous species were measured hourly using an AIM, and ion mass balance was used to ensure data quality under the quality control procedures of the AQM network installation and operation guidelines (NIER, 2021).

Aircraft measurements were conducted during the GMAP-2020 campaign period, and nine flights were conducted on 8 days (Nov. 26, 27, and 28 and Dec. 1, 6, 8, 9, and 12, 2020). The horizontal and vertical distributions of NO_2 and O_3 over Seosan were measured during GMAP-2020 using an NO_2 monitor (T500U; Teledyne, Thousand Oaks, CA, USA) and an O_3 analyzer (TEI49C; Thermo Scientific) onboard the Cessna Grand Caravan 208 B. These instruments had response times of <40 and <20 s, and detection limits of 40 ppt and 1 ppb, respectively. The flight paths included a raster mode over all of Seosan at a height of 500–700 m and a profiling mode from 500 m to 1.5 km over PA_1 and PA_4 (Fig. 2).

3.4 Meteorological measurements

Ground-based hourly observation data for meteorological variables were obtained from Seosan Automated Synoptic Observing System (ASOS) stations maintained by the KMA, and wind and temperature profile data were obtained twice daily (0000 and 1200 UTC) via a rawinsonde instrument at the Osan World Meteorological Organization upper air measurement station (47122) near Seosan. Due to time constraints of the sonde measurements, information on PBLH variation was obtained from Unified Model (UM) simulation results provided on the KMA website (https://afso.kma.go.kr).

During the GMAP-2020 campaign, a 3D sonic anemometer (CPEC200; Campbell Scientific, Logan, UT, USA) was also installed on the rooftop at PA_4 for turbulent flux measurements at the city–atmosphere interface (Hong *et al.*, 2019). All wind components and sonic temperatures were measured at a 10 Hz sampling rate, and ground-level sensitive heat flux was measured directly using a 30 min averaging period. Quality controls such as double rotation, spike removal, and outlier filtering were also applied.

3.5 Correlation analyses

We examined the synergy of PC and SI data obtained during the GMAP-2020 campaign, and combined these measurement data to evaluate air quality in Seosan, South Korea. We attempted to interpret the meteorological and photochemistry data measured during GMAP-2020, and to demonstrate that caution is required when attempting to study the vertical structure of air pollutants using either surface observations or satellite data only, particularly in industrial areas.

First, we examined the combined use of year-long PC-NO_2 and SI-NO_2 measurements, and investigated the factors modulating their correlation. Numerous studies have examined the correlations between chemical species, including aerosols (Thomspon et al., 2019; Wang et al., 2019; Kim et al, 2012; Jo et al., 2013; Sanchez et al., 1990; Kim et al, 2018). Wang *et al.* (2019) reported that aerosols moderately correlate with NO_2 due to the frequent occurrence of lifted layers probably related to the transport of pollutants. Jo *et al.* (2013) differentiated haze types using the trajectory speed and direction and different synoptic conditions. In this background, we hypothesized that their differences in PC-NO_2 and SI-NO_2 were due to meteorological conditions, and performed k-means and agglomerative hierarchical cluster analyses of various meteorological variables. Clustering is the grouping of objects that are alike and are different from the objects belonging to other clusters. As a first step, k-means Clustering was applied to find smaller clusters until each object was classified in one cluster. Subsequently, agglomerative hierarchical steps are applied to make up for the shortcomings of k-means clustering, in which once merging (or splitting) is done, it can never be undone. More details are found in Venkat Reddy *et al.* (2017). We used XLSTAT software (Addinsoft, Paris, France) for the cluster analysis with eight meteorological variables representing local and synoptic circulations in the cluster analysis: surface wind speed (Wsfc), 925 hPa temperature (T925), sea level pressure (Psfc), pressure tendency (dPsfc/dt), 850 hPa wind speed (W850) and its north–south and east–west components (NS850 and EW850), and 500 hPa geopotential height (GPH500). We subtracted 30-day moving averages from all data to account for typical seasonal variation. Monthly averages were used for PC-NO_2 analysis due to the limited availability of hourly data.

Correlations between PC-NO_2 and SI-NO_2 were analyzed in each meteorological group and the impact of photochemistry was interpreted based on case-specific features. We also investigated correlations in association with near-surface micrometeorological variables such as PBLH in each meteorological group.

4. Results and Discussion

4.1 Correlation analysis results for PC-NO_2 and SI-NO_2

The yearly PC-NO_2 statistics at four Pandora sites (PA_1–PA_4) are summarized in Table 1. The total averaged PC–NO_2 over all sites was 0.45 DU during GMAP-2020, which is well above the typical values (0.1–0.2 DU) for Anmyeondo (the location is shown in Figure 1), a representative background site (Herman *et al.*, 2018). Although site PA_3 is located in a rural area, it nevertheless exhibited the highest PC-NO_2 amounts, suggesting that plumes were frequently transported from nearby point sources and/or urban areas.

Scatter diagrams of hourly PC-NO_2 and SI-NO_2 measurements from Pandora sites PA_1–PA_3 (GMAP-2020) and PA_4 (yearly measurement; November 12, 2020–October 30, 2021) are shown in Fig. 3a. These hourly data had a fair logarithmic relationship (R = 0.45), and a relatively weaker 1:1 linear relationship (R = 0.41), where the linear relationship with PC-NO_2 weakened as SI-NO_2 levels increased. It appears that the SI-NO_2 has a distinct diurnal change despite the same PC-NO_2, and higher variable surface NO_2 levels may result from the relatively weaker linear relationship between PC-NO_2 and SI-NO_2. To explore these anti-correlation cases further, we selected the lower and upper bounds of the tendencies; these are plotted in Fig. 3b, which shows that PC-NO_2 was positively correlated with SI-NO_2 on February 24, 2021 (R = 0.88), while a negative correlation occurred on April 21, 2021 (R = –0.88), indicating a wide range of case-specific correlations. The negative correlation on April 21 (Fig. 3b) implied that the nonhomogeneous NO_2 distributions vertically were partially due to the photochemical process. For example, the decrease in PC-NO_2 despite an increase in SI-NO_2 might have occurred because NO_2 is removed by photochemical loss; it can occur more severely in the upper atmosphere with high OH concentrations. Another possible reason is the occurrence of lifted layers related to pollutant transport, yielding sharp changes in vertical concentration from the surface to the upper layer. The case-specific discussion follows.

Generally, in remote and clean regions such as the Pacific Ocean, local surface NO_2 concentrations are considered at background level, and can be used to represent stratospheric NO_2 amounts. The background level in our study would ideally correspond to the intercept of the regression model in the PC-SI NO_2 scatter diagram (Fig. 3a). In our analysis of yearly measurements, the intercept of 0.09 DU was consistent with stratospheric NO_2 column density (0.10 ± 0.02 DU) estimated during the GMAP campaign from the tropospheric monitoring instrument (TROPOMI) at a nadir pass time of approximately at 1330.

4.2 Impacts of meteorological conditions on correlations between PC-NO_2 and SI-NO_2

Our k-means cluster analysis distinguished three groups with the lowest within-group variance and largest among-group variance. Among the total of 141 cases, 47, 66, and 28 were classified into groups 1–3, respectively. Thus, group 2 had the largest proportion of cases (47%) and group 3 had the smallest (20%). The combination of meteorological components in group 1 indicated the end of a high-pressure system ($Psfc > 0$, $dPsfc/dt < 0$), with southerly winds ($NS850 > 0$) bringing warmer air ($T925 > 0$) to the region, leading to stable atmospheric stratification and weak surface winds (Fig. 4). This group 1 meteorological mode appeared to result in very weak NO_2 ventilation, which produced the highest PC-NO_2 and SI-NO_2 values. Group 3 showed the opposite trend, with strong northerly winds bringing colder air into the region, leading to an unstable atmosphere and stronger surface winds, and ultimately decreasing PC-NO_2 and SI-NO_2 to their lowest levels.

SI-NO_2 was approximately twice as high in group 1 than group 3, whereas PC-NO_2 showed no significant difference (Fig. 4a). We hypothesized that PBLH might also differ significantly under these micrometeorological conditions; therefore, we further explored daily maximum PBLH simulated by the Global Forecast System (GFS) and Lagrangian backward trajectories obtained from Hybrid Single-Particle Lagrangian Integrated Trajectory (HYSPLIT) and GFS system for the 141 cases. The mean simulated PBLH in Seosan, our study area, was 942.1 ± 405.3 m for 2020, which was similar to the annual mean daily maximum PBLH (1,013.6 m) in Osan (Lee *et al.*, 2013). However, the simulated PBLH differed significantly among the three groups (767.0 ± 304.8, 923.2 ± 335.3, and 1,280.6 ± 501.2 m for groups 1–3, respectively). The PBLH for group 3 was 1.7-fold higher than that for group 1 (Fig. 4k). We also detected significant differences among the three groups in synoptic components of the lower troposphere including W850, as well as in local meteorological parameters such as the sea breeze index (SBI) suggested by Biggs and Graves (1962), which is defined as, $\mathrm{SBI} = \frac{U^2}{C_p \Delta T}$, where U is Wsfc (Fig. 4c), C_p is specific heat, and ΔT is the temperature difference between T925 and the sea surface temperature. Thus, the SBI represents the ratio between inertial ($\rho U^2/2$) and buoyance forces ($\rho g C_p \Delta T$), where ρ is air density and g is gravity, and its value provides an indication of the likelihood of local circulation events such as sea breezes; at higher SBIs (i.e., SBI > 3), sea breezes cannot overcome the prevailing wind, whereas lower SBIs (i.e., 0 < SBI < 3) can indicate strong sea breezes.

In the example shown in Fig. 4l, the SBI for groups 1–3 was 0.1 ± 4.5, 0.1 ± 9.2, and –0.2 ± 12.5, respectively. Most SBIs in group 1 ranged from 0 to 3, indicating that group 1 corresponded to the dominant local circulation (LD), whereas the SBIs in group 3 had the lowest frequencies comparing 1 and 3, which corresponded to a dominant synoptic-scale circulation (SD). Group 2 can be considered a mixture of local and synoptic-scale circulation (MD). These results indicate that Seosan may experience frequent LD conditions (with sun on one third of the days of the year), with infrequent SD conditions (one fifth of all days).

4.2.1 Relationship between daily mean PC-NO_2 and SI-NO_2 under LD, MD, and SD

conditions

Scatter diagrams of daytime mean PC-NO_2 and SI-NO_2 measurements at Seosan over the entire 1-year period are shown in Fig. 5. Based on the 141 cases, daytime mean values averaged between 1100 and 1700 KST were used to reduce the effect of nocturnal PBLH variation. Other data selection criteria included concurrent PC-NO_2 and SI-NO_2 measurements, with data acquisition rates of >80% per day. Overall, PC-NO_2 and SI-NO_2 were strongly correlated (R = 0.73; Fig. 5), suggesting that the vertical profiles were generally uniform in the PBL throughout all four seasons. The slope of the linear regression curve shown in Fig. 5a was 0.02 DU/ppb (= 0.53×10^{15} molecules cm^{-2}/ppb), which is comparable to values ($0.3–0.59 \times 10^{15}$ molecules cm^{-2}/ppb) obtained previously in a study of surface and OMI-NO_2 measurements downwind of strong point sources in Israeli cities (Boersma *et al.*, 2009). The intercept (0.17 DU) was within the range of previous Anmyeondo Pandora measurements, suggesting that intercepts of 0.15–0.2 DU may represent the local background PC-NO_2 amount (including the stratospheric NO_2), rather than the influence of local anthropogenic NO_2 emissions.

We classified daily averaged PC-NO_2 and SI-NO_2 data according to the three meteorological conditions (LD, MD, and SD) and detected a weak correlation under LD conditions (Fig. 5b); the lowest coefficient of determination for the LD condition (R^2 = 0.34) was approximately half of those for the MD (0.359) and SD (0.64) conditions, suggesting that NO_2 vertical profiles were more complex under LD conditions, with anomalous layers.

4.2.2 Diurnal variation in column-surface NO_2 under LD, MD, and SD conditions

Diurnal patterns of PC-NO_2, SI-NO_2, and O_3 under SD, MD, and LD conditions are shown in Fig. 6. Under LD conditions, PC-NO_2 increased from morning to afternoon (Fig. 6a), whereas under SD conditions, it had a weak morning peak and subsequent decrease until late afternoon (Fig. 6c). Under MD conditions, PC-NO_2 had one large peak in the morning and a shoulder peak in the late afternoon (Fig. 6b). However, SI-NO_2 showed nearly identical diurnal patterns among the three meteorological conditions, with an early morning peak followed by a second peak in the late afternoon (Fig. 6d–f). Diurnal patterns of O_3 were strongly associated with O_3-NO_2 photochemical reactions under both LD and MD conditions (Fig. 6g–h), whereas no particular photochemical effects were detected under SD conditions (Fig. 6i).

A simple linear regression was applied to daytime average (1100–1700 LST) measurements of both PC-NO_2 and SI-NO_2 under the three meteorological conditions, and yielded correlation coefficients (R) of 0.51 and 0.41 for SD and MD conditions, respectively; however, LD conditions produced a significantly lower R (0.27). Thus, under SD conditions, strong synoptic winds suppressed PC-NO_2 and SI-NO_2 diurnal fluctuations, rendering them similar to each other. Strong winds also inhibited local effects of O_3 formation on the diurnal variation in PC-NO_2, and the smaller impact of chemical conversion from local NO_2 to O_3 lowered R values during the day. Under MD conditions, both PC-NO_2 and SI-NO_2 exhibited distinctive peaks in the morning with a degree of time lag; both subsequently declined toward noon, and showed higher R values than those obtained under SD conditions. By contrast, under MD conditions, correlations were enhanced due to a minimum around 1500 KST for both PC-NO_2 and SI-NO_2, despite time lags in both peaks in the morning and afternoon.

Previous studies of the Megacity Air Pollution Seoul (MAPS-Seoul) and KORUS-AQ campaigns reported a typical pattern of continuously increasing PC-NO_2 over the Seoul metropolitan area (Chong *et al.*, 2018; Herman *et. al.*, 2018). However, in the current campaign, we found similar results only under LD conditions. The diurnal patterns reported in previous studies were mainly caused by the dominance of NO_2 emissions sources over NO_2 losses (Chong *et al.*, 2018; Herman *et al.*, 2018) among several processes associated with NO_2 photochemical loss, including transport and deposition, which were also investigated in specific cases in the current study.

In this study, we extended the correlation analysis, and investigated the correlation between hourly PC-NO_2 and SI-NO_2 data. The results show a lower correlation in the morning, and a higher correlation in the afternoon (Fig. S1). The respective median correlation coefficients for the LD, MD, and SD meteorological conditions were -0.71, 0.18, and 0.22 in the morning (0900–1200 LST), and 0.84, 0.77, and 0.79 in the afternoon (1200–1400 LST). These values may reflect PBL development. SI-NO_2 decreases in the morning due to the rapid growth of the PBL, while PC-NO_2 increases due to the accumulation of NO_2 in the atmosphere, deriving a lower correlation. However, there is very little change in the PBL in the afternoon, and PC-NO_2 and SI-NO_2 show similar changes, yielding a positive correlation each other during the GMAP-2020 campaign.

4.3 Aircraft measurements collected during GMAP-2020

Data collected via aircraft during GMAP-2020 are summarized in Table 2. A total of nine aircraft measurements were conducted during the campaign period (November 12, 2020–January 20, 2021). Four of nine flights were conducted under LD conditions, and the remaining flights (except that on November 27, 2020) were conducted under MD conditions. No aircraft measurements were consistent with SD conditions during the GMAP-2020 campaign.

We examined spiral segments from each flight over Seosan during 1100–1700KST to exclude marginal effects of diurnal variation in NO_2 (Fig. 2). The overall results indicated that the vertical O_3 profiles were relatively constant in the PBL, whereas NO_2 profiles appeared to be highly dependent on meteorological conditions. We compared data collected during flights conducted under LD (one flight) and MD conditions (two flights) during the GMAP-2020 campaign, to examine differences in the vertical structures of the PA and SI observations.

Aircraft measurements of vertical NO_2 and O_3 profiles for flights FL-5 (December 6) and FL-6 (December 8) under LD conditions are shown in Fig. 7, along with 24 h backward trajectories starting at different altitudes (100, 500, and 1,000 m). All observed NO_2 profiles shown in Fig. 7 appeared to have generally exponential curves, with anomalous features at higher altitudes. For example, when vertical turbulent mixing prevailed within the PBL (O_3 profile, Fig. 7b), the data were fitted with an exponential vertical curve, and the anomalous NO_2 layer aloft was found to have a height of 1.5 km, which was higher than the estimated PBLH of 1.2 km. HYSPLIT 24 h backward trajectories starting at 1200 KST showed that all air mass from the surface to the lower free atmosphere was transported over the Yellow Sea via the Shandong Peninsula (Fig. 7c). This finding suggests that the anomalous NO_2 layer aloft was not produced locally (i.e., from local LPS emissions), but instead traveled via long-range regional-scale transport. This transport of NO_2 across the region was also discussed and might be particularly high during the winter when the NO_x lifetime is relatively longer (Stohl *et al.*, 2002; Wenig *et al.*, 2003; Lee *et al.*, 2013). According to Anmyeondo Lidar measurements for December 6 (http://kalion.kr), the anomalous NO_2 layer aloft corresponded well to an aerosol layer that appeared at ~1.0 km at approximately 1200 KST, persisting until 2200 KST. However, based on a cross-comparison of our data, high surface levels of SI-NO_2 (> ~4 ppb; Fig. 7a) were influenced more by local LPS than by that in the atmosphere aloft due to long-range transport (Fig. 7a).

Aircraft measurements for flight FL-7 (December 9) under LD conditions are shown in Fig. 7b. The NO_2 vertical profile exhibited an exponential curve, with an anomalous peak at ~600 m immediately above the top of the simulated PBL. HYSPLIT backward trajectory data starting at 1200 KST showed that the non-surface air had a different origin from the surface air (Fig. 6d), indicating that the anomalous NO_2 plume likely traveled from coal-fired power plants in a nearby industrial city (Taean) northwest of Seosan. This finding indicates a distinct vertical structure of higher NO_2 at the surface due to strong local emissions, whereas lower NO_2 levels were observed at higher altitudes, with anomalously high NO_2 levels in some layers aloft due to medium-range transport from nearby areas. Thus, despite the limited number of aircraft measurements, the elevated anomalous NO_2 structure that was observed intermittently led to a negative correlation between PA-NO_2 and SI-NO_2. The discrepancies imply that vertical profile distribution study should proceed cautiously when only surface measurements are obtained under LD meteorological conditions.

Aircraft measurements were conducted under MD conditions on flights FL-1 (November 26), FL-3 (November 28), and FL-8 (December 12) (Fig. 8). We applied several regression models (linear, exponential, and polynomial) to three vertical structures, and obtained two distinct NO_2 vertical profile patterns from the surface to the PBLH: decreasing linearly for FL-1 and FL-8 (Fig. 8), and constant with altitude for FL-3 (Fig. 8b). None of the three cases showed anomalous layers above the PBLH, similar to the exponentially declining profiles obtained under LD conditions (Fig. 7). These vertical structures observed under MD conditions may have been induced by strong vertical mixing within the PBL, supplemented by prominent surface photochemical losses at the same time. The vertical O_3 profile during FL-1 showed a decoupled structure, with different patterns within and above the PBL (Fig. 8d); however, the other 2 days showed uniform distributions, with no particular anomalous features between the upper PBL and surface atmosphere (Fig. 8b, c, e, f). The observed daily maximum sensible heat fluxes measured at Seosan (Fig. S3) were much higher for FL-3 (175.9 Wm^{-2}) than FL-1 and FL-8 (118.9 and 102.0 Wm^{-2}), suggesting that vertical turbulent mixing was much more prominent during FL-3. These chemical and physical characteristics are all related to MD conditions. Thus, the higher coefficient of determination (R^2 = 0.64) obtained under MD conditions (Fig. 5b) has an important bearing on the absence of irregular or anomalous layers aloft, with little variation regardless of the shape of the curve (Figs. 7 and 8).

4.4 Analyses of column–surface relationships for specific GMAP-2020 cases

Figure 9 shows examples of PC-NO_2 and SI-NO_2 diurnal variation under LD (FL-5 and FL-7) and MD (FL-1 and FL-8) conditions, and Fig. 10 shows latitudinal mean distributions for FL-5 and FL-7, based on the aircraft measurement data shown in Figs. 7 and 8. PC-NO_2 was decoupled from SI-NO_2 on 2 days, FL-5 and FL-7, which were both classified as having LD conditions (Fig. 9a, b), whereas good vertical mixing and uniform NO_2 distribution were observed on the remaining 2 days, FL-1 and FL-8, which showed MD conditions (Fig. 9c, d). According to our analysis of the aircraft measurements (Fig. 7), the poor correlations between PC-NO_2 and SI-NO_2 captured by FL-5 and FL-7 were mainly due to an NO_2 polluted layer transported aloft, as described in Section 4.3.

4.4.1 LD conditions

Several cases showed poor correlations between PC-NO_2 and SI-NO_2 under LD conditions within the study period. When we examined the results of previous studies (Thompson et al., 2019; Chong et al., 2018; Herman et al., 2018; Kim et al., 2021), we first considered the possibility that LPS emissions influenced downwind regions under LD conditions, because the increase in PC-NO_2, but not SI-NO_2, may have required an additional source of NO_2 apart from early afternoon traffic emissions. The FL-5 data for December 6 represent an example of this, showing a poor correlation between PC-NO_2 and SI-NO_2 (R^2 = 0.06; Fig. 9a). On the same day, Anmyeondo LIDAR detected two elevated aerosol layers at 1200 and 1600–2200 KST (http://kalion.kr); the first aerosol layer may reflect a PC-NO_2 peak, as shown in Fig. 9a. The HYSPLIT backward trajectories, starting at different altitudes from the surface to the lower troposphere, revealed that all air parcels moved eastward from China to Anmyeondo and Seosan (Figure 1); thus, other NO_2 plumes may have begun to pass over Seosan at 1600KST (Fig. 7c). Longitudinal SI-NO_2 distributions (Fig. 10) exhibited 5.2 ppb at 126.1°E, 8.1 ppb at 126.3°E, and 7.3 ppb at 126.4°E, averaged between 1300 and 1600 KST by longitude (Table

S1), whereas they were nearly constant at a height of 500–600 m on December 6. Therefore, westerly winds advected cleaner air from Padori (AQM_1) to Seosan at the surface, but not at a height of 500–600 m, contributing to low SI-NO_2 levels in the afternoon (Fig. 9a).

Another example of a weak correlation was obtained by flight FL-7 (December 9), as shown in Fig. 9b. Time series PC-NO_2 data exhibited several peaks during 1200–1400 KST (Fig. 9b), whereas SI-NO_2 showed less temporal variation, resulting in a weak correlation (R = –0.24) compared to the overall daytime (1100–1700 KST) correlation ($R^2 = 0.53$; Fig. 5a). Latitudinal NO_2 levels at high altitudes of ~600 m (Fig. 10b) gradually increased northward, whereas surface NO_2 was minimal at the midpoint. For example, at high altitudes, the latitudinal mean NO_2 levels were 1.4 ppb (36.8°N), 4.1 ppb (36.9°N), and 5.1 ppb (37.0°N), whereas the SI-NO_2 levels at the same sites were 18.0 ppb (36.8°N), 14.3 ppb (36.9°N), and 16.8 ppb (37.0°N), respectively, averaged during 1200–1400 KST by latitude (Table S1). This finding is attributable to a prevailing north wind that transported NO_2 southward at high altitudes, while simultaneously ventilating SI-NO_2 toward outer Seosan, resulting in the development of several PC-NO_2 peaks. By contrast, SI-NO_2 decreased slowly (Figs. 9b and 10b).

4.4.2 MD and SD conditions

We obtained higher PC–SI correlation coefficients under MD and SD conditions than LD conditions (Figs. 5b and 9c, d). Under MD and SD conditions, diurnal variation in PC-NO_2 and SI-NO_2 showed simultaneous declines from early morning until noon (Fig. 6). Notably, PC-NO_2 showed a continuously decreasing trend, particularly during the morning hours, in the period of approximately 0900–1200 KST under both MD and SD conditions (Fig. 6b, c). These diurnal patterns of decreasing PC-NO_2 in the study area were opposite to those reported in previous studies (Chong *et al.*, 2018; Herman *et al.*, 2018) that observed increasing PC-NO_2 in large urban areas during the daytime, caused by higher NO_2 emissions even during photochemical NO_2 losses to form O_3.

We hypothesized that decreasing PC-NO_2 can occur due to photochemical loss and surface wind transport, which both intensify with increasing solar radiation in the morning. Photochemically, NO_2 is converted into photochemical oxidants such as PAN, HNO_3, and nitrate under sunlight, thereby disrupting the NOx–VOC–O_3 cycle. Concurrently, Wsfc intensified due to thermal turbulence transport of NO_2 emissions away from Seosan during the day. Thus, PC-NO_2 decreases under MD conditions as a result of ventilation effects caused by stronger wind speeds. There are two possible mechanisms for this: sea breeze penetration (because the study area is adjacent to the northern coast of the Taean Peninsula; Fig. 1) and vigorous turbulent mixing (which leads to vertical mixing of surface NO_2 during PBL growth; Sun *et al.*, 2013). We investigated these factors in detail for specific cases.

Figure 11 shows the diurnal variation in selected meteorological and chemical variables measured under MD (November 25) and SD conditions (December 14). Under MD conditions (Fig. 11a–c), declines in PC-NO_2 and SI-NO_2 were observed toward noon. In particular, decreasing PC-NO_2 was accompanied by increased Wsfc (Fig. 11b); therefore, we examined GMAP-2020 campaign measurements of sea breeze penetration. Figure S2a shows diurnal variation in observed air temperatures at site Met_1 and measured sea surface temperatures at nearby site Met_2 (37.14°N, 126.01°E), located 55 km from PA_4. The thermal meteorological observations were used to calculate SBI (+0.37), which was greater than +3 (the threshold for sea breeze occurrence; Brigges and Graves, 1962). Sea breeze disturbances with a sharp decrease (increase) in temperature (humidity) were observed at site Met_3 (Fig. S3b), which is located on the northern coastline of Taean Peninsula (Fig. 1). However, sea breezes did not progress inland at the Met_1 Seosan Meteorological Automated Surface Observing System (ASOS) site, which is closer to the Pandora sites; sea breezes did not correlate with NO_2

ventilation to offset its high emission.

We further detected a strong positive correlation between wind speed and sensible heat flux (Fig. 11b). We speculated that thermal and momentum turbulences caused by a vertical temperature gradient and surface friction entrained surface turbulence, thus increasing momentum in the free atmosphere downward to the surface due to strong turbulent mixing within the PBL, in turn leading to a uniform vertical NO_2 profile with a positive correlation between PC-NO_2 and SI-NO_2. Figure S3 shows a comparison of daily maximum sensible heat and momentum fluxes under LD, MD, and SD conditions during the GMAP-2020 campaign. SD conditions showed the highest mean heat flux, followed by MD and LD, indicating that downward momentum transport led by both heat and momentum fluxes plays a greater role in Wsfc enhancement under MD than LD conditions within the PBL.

Photolytic NO_2 loss was detected as temporal variation in NO_2, $NO_3^–$, and CO at PA_4. Because no NO_2 analyzer was installed at PA_4, NO_2^*(= NO_y–NO) was used instead of NO_2 under the assumption that NO_z is negligible in winter. Figure 11c shows the diurnal variation in NO_2, O_3, and $NO_3^–$ under MD conditions, normalized by CO to reduce the effect of PBL evolution. The results showed that NO_2/CO decreased after the morning peak; however, $NO_3^–$ /CO and O_3/CO increased toward midday, indicating that photolytic activity also contributed considerably to the concurrent decline of SI-NO_2 and PC-NO_2 (Fig. 11a). In turn, this indicated that photochemistry can contribute to higher correlation coefficients under MD conditions.

Under SD conditions (Fig. 11d–f), PA-NO_2 and SI-NO_2 exhibited weak diurnal variability compared to LD and MD conditions. SD conditions on December 14 produced significantly stronger winds (i.e., wind speed > 6 m $s^{–1}$ at 1300 KST), with generally higher PBLHs (Fig. 11e). Meteorological features, such as strong wind at both 850 hPa (18.0 m $s^{–1}$) and 10 m height (4.26 m $s^{–1}$), suppressed both PC-NO_2 and SI-NO_2 (7.3 ppb and 0.31 DU, respectively) to below the average, producing a strong correlation (R = 0.9 at AQM_5) and nearly flattening their temporal curves during the day (Fig. 11d). Thus, under SD conditions, wind speed and turbulent fluxes such as sensible heat flux had larger values, and NO_2 and NO_3^- decreased or increased at the same time during the day (Fig. 11f), indicating that the transport effect was much greater than that of local photochemical loss over the study area.

In conclusion, in this case-specific study, we assessed the correlations between PC-NO_2 and SI-NO_2, and explored their mechanisms by investigating the impact of meteorological and photochemical conditions. A weak correlation between PC-NO_2 and SI-NO_2 occurred when anomalously high concentrations remained, with ragged fragments of NO_2 plumes in the upper or middle layers. We also found that a negative correlation occurred intermittently under LD conditions, with generally lower PBLH. In particular, elevated pollutant levels due to regional-scale transport or decoupled NO_2 plumes advected within the PBL may have also caused the weak correlation between PC-NO_2 vs. SI-NO_2. These phenomena were detected only from the PA–SI coupled measurements in this study. Thus, when either PC or SI observations are applied alone for understanding the vertical structure of air pollutants, undetected bias can occur under LD conditions, particularly where transport processes prevail, and these results can be also applicable to GEMS observations analysis.

5. Conclusion

We explored the potential applicability of combined PC-NO_2 and SI-NO_2 measurements collected at Seosan during the GMAP-2020 campaign. We characterized the correlation between PC-NO_2 and SI-NO_2 under various conditions to understand the complex air quality of Seosan, which appears to be vulnerable to LPS emissions from surrounding areas. We hypothesize that correlations between PC-NO_2 and SI-NO_2 are closely related to NO_2 vertical profiles, which also depend on meteorological conditions. We performed statistical analyses of a year-long PC-NO_2 dataset (November 12, 2020–October 30, 2021) combined with meteorological data, *in situ* ground data, and airborne chemical data measured during the GMAP-2020 campaign in the same period.

Our results show that hourly PC-NO_2 and SI-NO_2 over the 1-year period exhibited a logarithmic relationship with a fair correlation (R = 0.45), and the intercept of the logarithm regression line (corresponding to zero-surface NO_2) was 0.09 DU, consistent with the stratospheric column NO_2 amounts retrieved by TROPOMI. Daily mean PC-NO_2 and SI-NO_2 exhibited a good linear correlation (R = 0.73), supporting the overall uniformity of NO_2 profiles in the PBL over Seosan despite the continuous impact of LPS emissions.

The impact of meteorological conditions on the relationship between PC-NO_2 and SI-NO_2 was investigated through agglomerative hierarchical clustering, which indicated three meteorological conditions: LD, MD, and SD. Under LD conditions, southerly winds advect warm air under the upper ridge, forming stable and short PBLs and weak surface winds. By contrast, under SD conditions, cold northerly winds induce unstable and high PBLs with strong surface winds. The correlations between daily mean PC-NO_2 and SI-NO_2 levels, and their variation during 1100–1700 KST, weakened under LD conditions, suggesting that the shape of the NO_2 profile typically deviates from a uniform profile under SD and MD conditions. Aircraft measurements under LD conditions demonstrated NO_2 plumes aloft, with anomalous vertical structures and different horizontal (latitudinal) gradients of surface NO_2 at higher altitudes, such as 600 m over Seosan.

Thus, the relationship between PC-NO_2 and SI-NO_2 depends on the presence of NO_2 plumes aloft under LD conditions, which provide a favorable environment for LPS plumes decoupled from the surface at Seosan. Our findings suggest that the correlation between PC-NO_2 and SI-NO_2 may serve as an indicator of the degree of complexity of urban air quality. This correlation can be optimally applied for air quality evaluation and vertical analysis by combining the Pandora Asia Network with AQM networks, and the results can be also applied to environmental GEMS observation analysis in combination with SI observations. More detailed studies on urban air pollution evaluation will be undertaken based on PC, DOAS, aircraft, SI air quality, and surface turbulence observation data, as well as modeling studies of data collected during the GMAP-2021 campaign.

Acknowledgments

We thank all those who contributed to the GMAP-2020 field campaign, NASA GSFC for use of Pandora instruments, and PGN for raw data processing.

Funding.

This study was supported by the National Institute of Environmental Research (NIER-2021-01-01-052 and NIER-2021-03-03-001), and was partially supported by National Research Foundation of Korea (NRF) funded by the Ministry of Education of the Republic of Korea (Grant No. 2020R1I1A2075417)

Data Availability.

The measurements can be accessed by contacting the corresponding authors.

Competing interest.

The authors declare that they have no conflict of interest.

Author Contributions.

Lim-Seok Chang: Conceptualization, Formal analysis, Visualization, Investigation, Writing - Original draft; Donghee Kim, Hyunkee Hong, Deok-Rae Kim, Jeonga Yu, and Daewon Kim; Data curation; Hanlim Lee, Kwangyul Lee, and Jinkyu Hong: Methodology and formal analysis; Hyun-

Young Jo: Formal analysis and Visualization; Cheol-Hee Kim ; Writing—original draft preparation, Writing—review and editing. All authors have read and agreed to the published version of the manuscript.

References

Biggs, W.G. and Graves, M.E.: A lake breeze index, J. Appl. Meteor., 1, 474–480, http://www.jstor.org/stable/26169480, 1962.

Boersma, K.F., Jacob, D.J., Trainic, M., Rudich, Y., DeSmedt, I., Dirksen, R., and Eskes, H.J.: Validation of urban NO_2 concentrations and their diurnal and seasonal variations observed from the SCIAMACHY and OMI sensors using in situ surface measurements in Israeli cities. Atmos. Chem. Phys., 9, 3867–3879, https://doi.org/10.5194/acp-9-3867-2009, 2009.

Cede A.: Manual for Blick Software Suite 1.7, Tech. rep., LuftBlick, Austria, 161 pp., 2019.

Chong, H., Lee, H., Koo, J.H., Kim, J., Jeong, U., Kim, W., Kim, S.W., Herman, J.R., Abuhassan, N.K., Ahn, J.Y., Park, J.H., Kim, S.K., Moon, K.J., Choi, W.J., and Park, S.S.: Regional characteristics of NO_2 column densities from Pandora observations during the MAPS-Seoul campaign, Aerosol Air Qual. Res. 18, 2207–2219, https://doi.org/10.4209/aaqr.2017.09.0341, 2018.

Engel-Cox, J.A., Holloman, C.H., Coutant, B.W., and Hoff, R.M.: Qualitative and quantitative evaluation of MODIS satellite sensor data for regional and urban scale air quality, Atmos. Environ., 38, 2495–2509, http://dx.doi.org/10.1016/j.atmosenv.2004.01.039, 2004.

Flynn, C.M., Pickering, K.E., Crawford, J.H., Weinheimer, A.J., Diskin, G., Thornhill, K.L., Loughner, C., Lee, P., and Strode, S.A.: Variability of O_3 and NO_2 profile shapes during DISCover-AQ: Implications for satellite observations and comparisons to model-simulated profiles, Atmos. Environ., 147, 133–156, https://doi.org/10.1016/j.atmosenv.2016.09.068, 2016.

Herman, J., Cede, A., Spinei, E., Mount, G., Tzortziou, M., and Abuhassan, N.: NO_2 column amounts from ground-based Pandora and MFDOAS spectrometers using the direct-sun DOAS technique:

Intercomparisons and application to OMI validation, J. Geophys. Res. Atmos, 114, D13307, https://doi.org/10.1029/2009JD011848, 2009.

Herman, J., Spinei, E., Fried, A., Kim, J., Kim, J., Kim, W., Cede, A., Abuhassan, N., and Rozenhaimer, S.M.: NO_2 and HCHO measurements in Korea from 2012 to 2016 from Pandora spectrometer instruments compared with OMI retrievals and with aircraft measurements during the KORUS-AQ campaign, Atmos. Meas. Tech., 11, 4583–4603, https://doi.org/10.5194/amt-11-4583-2018, 2018.

Hong, J.-W., Lee, S.-D., Lee, K., and Hong, J.: Seasonal variations in the surface energy and CO_2 flux over a high-rise, high-population, residential urban area in the East Asian monsoon region, Int. J. Climatol., 40, 4384–4407, https://doi.org/10.1002/joc.6463, 2019.

Jo, H.-Y. and Kim, C.-H: Identification of long-range transported haze phenomena and their meteorological features over Northeast Asia, J. Appl. Meteorol. Climatol., 52(6), 1318–1328, https://doi.org/10.1175/JAMC-D-11-0235.1, 2013.

Kim, C.-H., Lee, H.-J., Kang, J.-E., Jo, H.-Y., Park, S.-Y., Jo, Y.-J., Lee, J.-J., Yang, G.-H., Park, T., and Lee, T.: Meteorological Overview and Signatures of Long-range Transport Processes during the MAPS-Seoul 2015 Campaign, Aerosol Air Qual. Res., 18, 2173–2184, https://doi.org/10.4209/aaqr.2017.10.0398, 2018.

Kim, C.-H., Park, S.-Y., Kim, Y.-J., Chang, L.-S., Song, S.-K., Moon, Y.-S., and Song, C.-K.: A Numerical Study on Indicators of Long-range Transport Potential for Anthropogenic Particle Matter over Northeast Asia, Atmos. Environ., 58, 35–44, https://doi.org/10.1016/j.atmosenv.2011.11.002, 2012.

Kim, J., Jeong, U., Ahn, M.-H., Park, R.J., Lee, H., Song, C.H., Choi, Y..-S., Lee. K.-H. Yoo, J.-M., Jeong. M.-J. Park, S.K., Lee, K.-M., Song, C.-K., Kim, S.-W., Kim, Y.J., Kim, S.-W., Kim, M., Go, S., Liu, X., Chance, K., Miller, C.C., Al-Saadi, J., Veihelmann, B., Bhartia, P.K., Torres, O., Abad, G.G., Haffner, D.P., Ko, D.H., Lee, S.H., Woo, J.-H., Chong, H., Park, S.S., Micks, D., Choi, W.J., Moon, K.-J., Veefkind, P., Levelt, P.F., Edwards, D.P., Kang, M., Eo, M., Bak, J., Baek, K., Kwon, H.-A., Yang, J., Park, J., Han, K.M., Kim, B.-R., Shin, H.-W., Choi, H., Lee, E., Chong, J., Cha, Y., Koo, J.-H., Hayashida, S., Kasai, Y., Kanaya, Y., Liu, C., Lin, J., Crawford, J.H., Carmichael, G.R., Newchurch, M.,J., Lefer, B.L., Herman, J.R., Swap, R.J., Lau, A.K.H., Kurosu, T.P., Jaross, G., Ahlers, B., Dobber, M., McElroy, T.C.., and Choi, Y.: New era of air quality monitoring from space: Geostationary Environment Monitoring Spectrometer (GEMS), Bulletin of the American Meteorological Society, 101(1), E1-E22, https://doi.org/10.1175/BAMS-D-18-0013.1, 2020.

Kim, S.-U., Kim, K.-Y.: Physical and chemical mechanisms of the daily-to-seasonal variation of PM_{10} in Korea. Sci. Total Environ., 712, 136429, https://doi.org/10.1016/j.scitotenv.2019.136429, 2020.

Kim, S.-M., Koo, J.-H., Lee, H., Mok, J., Choi, M., Go, S., Lee, S., Cho, Y., Hong, J., and Seo, S.: Comparison of $PM_{2.5}$ in Seoul, Korea Estimated from the Various Ground-Based and Satellite AOD, Appl. Sci., 11(22), 10755, https://doi.org/10.3390/app112210755, 2021.

Lamsal, L.N., Martin, R.V., van Donkelaar, A., Celarier, E.A., Bucsela, E.J., Boersma, K.F., Dirksen, R., Luo, C., and Wang, Y.: Indirect validation of tropospheric nitrogen dioxide retrieved from the OMI satellite instrument: Insight into the seasonal variation of nitrogen oxides at northern midlatitudes, J. Geophys. Res., 115, D05302, https://doi.org/10.1029/2009JD013351, 2010.

Lee, S., Kim, M., Kim, S.Y., Lee, D.W., Lee, H., Kim, J., Le, S., and Liu, Y.: Assessment of long-range transboundary aerosols in Seoul, South Korea from Geostationary Ocean Color Imager (GOCI) and ground-based observations, Environ. Pollut., 269, 115924, https://doi.org/10.1016/j.envpol.2020.115924, 2021.

Lee, S.J., Lee, J., Greybush, S.J., Kang, M., and Kim, J.: Spatial and temporal variation in PBL height over the Korean Peninsula in the KMA operational regional model, Adv. Meteorol., 2013(10), 1-16, https://doi.org/10.1155/2013/381630, 2013.

National Institute of Environmental Research (NIER): Air Quality Monitoring Network Installation and Operation. Ministry of the Environment, Seoul, Korea, 2021.

Sanchez, M.L., Pascual, D., Ramos, C. and Perez, I.: Forecasting particulate pollutant concentrations in a city from meteorological variables and regional weather patterns, Atmos. Environ, 6, 1509–1519, https://doi.org/10.1016/0960-1686(90)90060-Z, 1990.

Stohl, A., Eckhardt, S., Forster, C., James, P., and Spichtinger, N.: On the pathways and timescales of intercontinental air pollution transport, J. Geophys. Res., 107(D23), 4684, doi:10.1029/2001JD001396, 2002.

Sun, J., Lenschow, D.H., Mahrt, L., and Nappo, C.: The relationships among wind, horizontal pressure gradient, and turbulent momentum transport during CASES-99, J. Atmos. Sci., 70, 3397–3414, http://dx.doi.org/10.1175/JAS-D-12-0233.1, 2013.

Thompson, A.M., Stauffer, R.M., Boyle, T.P., Kollonige, D.E., Miyazaki, K., Tzortziou, M., Herman, J.R., Abuhassan, N., Jordan, C.E., and Lamb, B.T.: Comparison of near-surface NO_2 pollution with Pandora total column NO_2 during the Korea-United States Ocean Color (KORUS OC) Campaign, J. Geophys. Res. Atmos.,124, 13560–13575, https://doi.org/10.1029/2019JD030765, 2019.

Van Roozendael, M. and Fayt, C.: WinDOAS Software user manual, Tech. rep., IASB/BIRA, Uccle, Belgium, http://uv-vis.aeronomie.be/software/WinDOAS, 2001.

Venkat Reddy M., Vivekananda M. and Satish RUVN: Divisive Hierarchical Clustering with K-means and Agglomerative Hierarchical Clustering, International Journal of Computer Science Trends and technology, 5(5), 6–12, doi:10.17485/ijst/2016/v9is1/96012, 2017.

Wang, J., and Christopher, S.A.: Intercomparison between satellite-derived aerosol optical thickness and $PM_{2.5}$ mass: Implications for air quality studies, Geophys. Res. Lett., 30, 2095, https://doi.org/10.1029/2003GL018174, 2003.

Wang, Y., Dörner, S., Donner, S., Böhnke, S., Smedt, I.D., Dickerson, R.R., Dong, Z., He, H., Li, Z., Li, D., Ren, X., Theys, N., Wang, Y., Wang, Z., Xu, H., Xu, J., and Wagner, T.: Vertical profiles of NO_2, SO_2, HONO, HCHO, CHOCHO and aerosols derived from MAX-DOAS measurements at a rural site in the central western North China Plain and their relation to emission sources and effects of regional transport, Atmos. Chem. Phys., 2, 5417–5449, http://dx.doi.org/10.5194/acp-19-5417-

2019, 2019.

Wenig, M., Spichtinger, N., Stohl, A., Held, G., Beirle, S., Wagner, T., Jahne, B., and Platt, U.: Intercontinental transport of nitrogen oxide pollution plumes, Atmos. Chem. Phys., 3, 387–393, SRef-ID: 1680-7324/acp/2003-3-387, 2003.

Zhao, X., Griffin, D., Fioletov, V., McLinden, C., Davies, J., Ogyu, A., Lee, S. C., Lupu, A., Moran, M. D., Cede, A., Tiefengraber, M., and Müller, M.: Retrieval of total column and surface NO_2 from Pandora zenith-sky measurements, Atmos. Chem. Phys., 19, 10619–10642, https://doi.org/10.5194/acp-19-10619-2019, 2019.

List of Tables

Table 1. Summary of NO$_2$ column data from four Pandora (PA) measurement sites.

Site	Site name	Site location		Mean (DU)	SD (DU)	Minimum (DU)	Maximum (DU)	Number of data points (days)	Operating period
		Longitude (°E)	Latitude (°N)						
PA$_1$	Seosan-DHJ	126.502	36.900	0.50	0.22	0.20	1.60	838 (11)	GMAP-2020 campaign
PA$_2$	Seosan-DM	126.458	36.778	0.43	0.19	0.18	1.62	1241 (13)	GMAP-2020 campaign
PA$_3$	Seosan-CC	126.449	36.785	0.40	0.14	0.18	0.97	1242 (13)	GMAP-2020 campaign
PA$_4$	Seosan-SS	127.492	36.777	0.39	0.16	0.17	1.79	8753 (141)*	1 year (Nov. 12, 2020–Oct. 30, 2021)

* The Pandonia Global Network (PGN) retrieval algorithm was applied to yearly measurements.

Table 2. Summary of aircraft measurements collected during the Geostationary Environment Monitoring Spectrometer (GEMS) Map of Air Pollution (GMAP)-2020 campaign period (November 12, 2020–January 20, 2021).

Flight no.	Date	Meteorological classification
FL-1	Nov. 26, 2020	MD [1]
FL-2	Nov. 27, 2020	No Pandora measurements
FL-3	Nov. 28, 2020	MD
FL-4	Dec. 1, 2020	LD[2]
FL-5	Dec. 6, 2020	LD
FL-6	Dec. 8, 2020	LD
FL-7	Dec. 9, 2020	LD
FL-8	Dec. 12, 2020 (am)	MD
FL-9	Dec. 12, 2020 (pm)	MD

[1] LD: local wind-dominant conditions; [2] MD: mixed conditions.

Figure Captions

Figure 1. Map of sites used for Geostationary Environment Monitoring Spectrometer (GEMS) Map of Air Pollution (GMAP) campaigns conducted in (left) Seosan, South Korea in November 2020 to January 2021 (GMAP-2020), and (right) the Seoul metropolitan area from October 2021 to November 2021 (GMAP-2021). (Left) Measurement sites around Seosan, the study area for the GMAP-2020 campaign. Red circles indicate Pandora column measurement sites including (left) Seosan Daehoji (PA_1), Seosan Dongmun (PA_2), Seosan City Council (PA_3), and Seosan Super Site (PA_4). Blue triangles indicate large point sources (LPSs) including the Taean and Dangjin thermal power stations (LPS_1 and LPS_2, respectively), Hyundai steelworks (LPS_3), and Daesan petrochemical complex (LPS_4). Yellow squares indicate Automated Synoptic Observing System meteorological sites in Seosan (Met_1), AWS (Met_2), and buoy (Met_3). Green squares indicate air quality monitoring (AQM) network stations including Padori (AQM_1), Leewon (AQM_2), Taean (AQM_3), Daesan (AQM_4), Seongyeon (AQM_5), and Dongmoon (AQM_6). In the right panel, the black line indicates the route used for car-based differential optical absorption spectroscopy (Car-DOAS) measurements and the blue dotted line indicates the horizontal domain of Geo-CAPE airborne simulator (GCAS) measurements taken during the GMAP-2021 campaign.

Figure 2. Flight tracks for two Cessna Grand Caravan 208 B aircraft over Pandora sites (left) PA_4 and (right) PA_1 during the GMAP-2020 campaign. Colored circles indicate airborne NO_2 concentration observations. Stacked circles indicate spiral flights conducted over two sites.

Figure 3. (a) Pandora column (PC) NO_2 measurements as a function of surface *in situ* (SI) NO_2 observations at Pandora sites PA_1–PA_3 during the GMAP-2020 campaign and PA_4 during a 1-year period. A logarithmic regression model was used to evaluate the relationship between PC and SI measurements (black line). (b) Samplescatter plots of PC-NO_2 and SI-NO_2 for February 24 (red) and April 21 (blue), 2021.

Figure 4. K-means clustering yielded three groups of cases for (a) surface NO_2 and (b) PC-NO_2, associated with eight meteorological variables: (c) surface wind speed (Wsfc), (d) Psfc, (e) Psfc tendency (dPsfc/dt), (f) 925-hPa air temperature (T925), (g) 850-hPa wind speed (W850), (h) 850-hPa north–south wind component (NS850), (i) 850-hPa east–west wind component (EW850), and (j) 500-hPa geopotential height (GPH500). All data were de-

seasonalized using the 30-day moving average, except PC-NO_2, for which the monthly average was used. (k) Simulated daily maximum mixing height (not directly clustered). (l) Box and whisker plots of the sea breeze index (SBI) at Seosan for the 1-year period. Red dots indicate the critical SBI (a value of 3), suggested by Biggs and Graves (1962).

Figure 5. (a) Scatterplots of daytime measurements at site PA_4 (a) PC-NO_2 vs. SI-NO_2 under all meteorological conditions and (b) PC-NO_2 vs. Surface $\triangle NO_2$ in each meteorological condition over a 1-year period (November 12, 2020–October 30, 2021). Here Surface $\triangle NO_2$ = SI-NO_2–(30-day moving average) SI-NO_2.

Figure 6. Box and whisker plots of diurnal variation in (a–c) PC-NO_2, (d–f) SI-NO_2, and (g–i) surface O_3 under synoptic wind-dominant (SD), mixed (MD), and local wind-dominant (LD) conditions in Seosan during a 1-year period (November 12, 2020–October 30, 2021).

Figure 7. Box and whisker plots of the vertical NO_2 and O_3 profiles measured by GMAP aircraft superposed with *in situ* $AQMS_1$ measurements during flights (a, b) FL-5 (December 6) and (d, e) FL-7 (December 6 and 9). Blue dashed lines are linear regression lines fitted to NO_2 and O_3 profiles within the planetary boundary layer (PBL). Black arrows indicate the simulated PBL height (PBLH) obtained from the Korea Meteorological Administration (KMA). HSYPLIT 24-h backward trajectories in Seosan are shown at altitudes of 100, 500, and 1,000 m, starting at 1600 KST on November 26 and 1200 KST on December 12.

Figure 8. Box and whisker plots of vertical profiles obtained from GMAP aircraft superposed with *in situ* AQMS measurements for (1) NO_2 and (2) O_3 for flights (a) FL-1 (November 26), (b) FL-3 (November 28), and (c) FL-8 (December 12). Blue dashed lines are linear regression lines fitted to NO_2 and O_3 in the PBL. Black arrows indicate PBLH simulated by the Hybrid Single-Particle Lagrangian Integrated Trajectory (HYSPLIT) Global Forecast System (GFS).

Figure 9. Time series and scatterplots of PC-NO_2 and SI-NO_2 at PA_2 on (a) December 6, (b) December 9, (c) November 26, and (d) December 12. (e) Scatterplot of PC-NO_2 and SI-NO_2 on December 6 (blue), December 9 (red), November 26 (gray), and December 12 (black). (f) Vertical potential temperature profiles on December 6, 9, and 12, 2020. Radiosonde data for November 26, 2020 are missing.

Figure 10. Latitudinal NO_2 distribution at the surface and 600 m over PA_4 (Seosan Super Site), averaged during (a) 1300–1600 KST on December 6 (FL-5) by longitude and (b) 1200–1400 KST on December 9 (FL-7) by latitude, obtained from airborne (blue) and surface measurements (red).

Figure 11. Examples of the diurnal variation on November 25 (a, c, e) and December 14 (b, d, f). (a, b) Column NO_2 at sites PA_1–PA_4 and surface NO_2 at air quality monitoring sites AQM_4 and AQM_6. (c, d) Sensible heat fluxes and surface wind speed at PA_4. (e, f) Diurnal variation in NO_2, NO_2^-, and O_3 normalized by CO. Figure 1 shows the locations of the measurement sites.

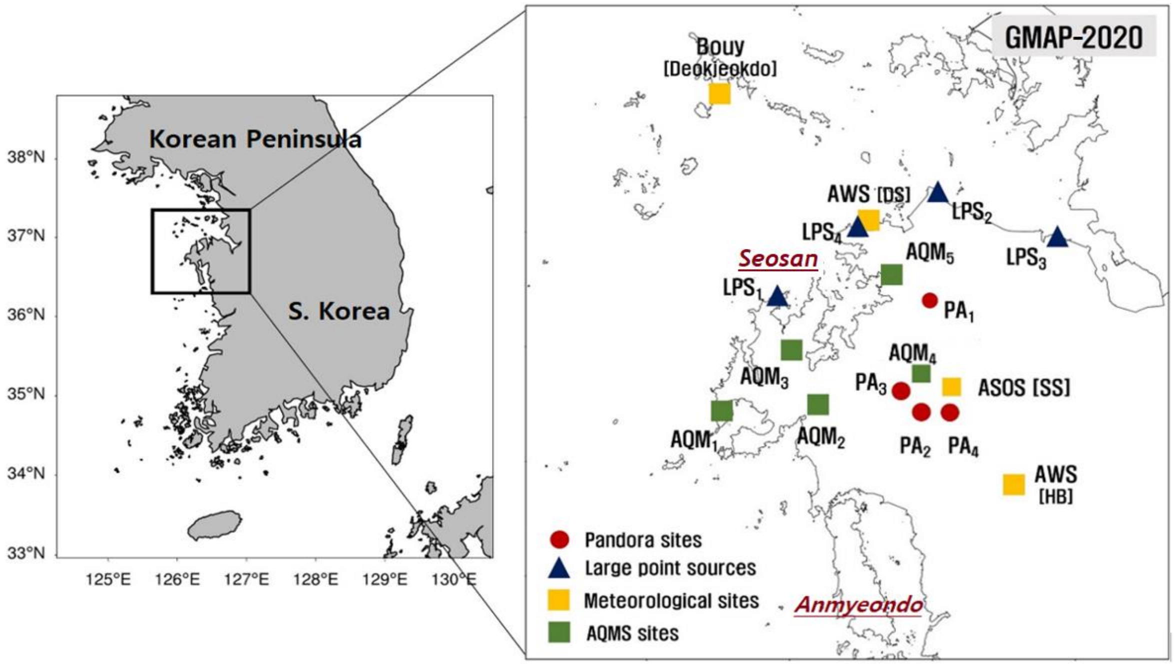

Figure 1. Map of sites used for Geostationary Environment Monitoring Spectrometer (GEMS) Map of Air Pollution (GMAP) campaigns conducted in (left) Seosan, South Korea in November 2020 to January 2021 (GMAP-2020), and (right) the Seoul metropolitan area from October 2021 to November 2021 (GMAP-2021). (Left) Measurement sites around Seosan, the study area for the GMAP-2020 campaign. Red circles indicate Pandora column measurement sites including (left) Seosan Daehoji (PA_1), Seosan Dongmun (PA_2), Seosan City Council (PA_3), and Seosan Super Site (PA_4). Blue triangles indicate large point sources (LPSs) including the Taean and Dangjin thermal power stations (LPS_1 and LPS_2, respectively), Hyundai steelworks (LPS_3), and Daesan petrochemical complex (LPS_4). Yellow squares indicate Automated Synoptic Observing System meteorological sites in Seosan (Met_1), AWS (Met_2), and buoy (Met_3). Green squares indicate air quality monitoring (AQM) network stations including Padori (AQM_1), Leewon (AQM_2), Taean (AQM_3), Daesan (AQM_4), Seongyeon (AQM_5), and Dongmoon (AQM_6). In the right panel, the black line indicates the route used for car-based differential optical absorption spectroscopy (Car-DOAS) measurements and the blue dotted line indicates the horizontal domain of Geo-CAPE airborne simulator (GCAS) measurements taken during the GMAP-2021 campaign.

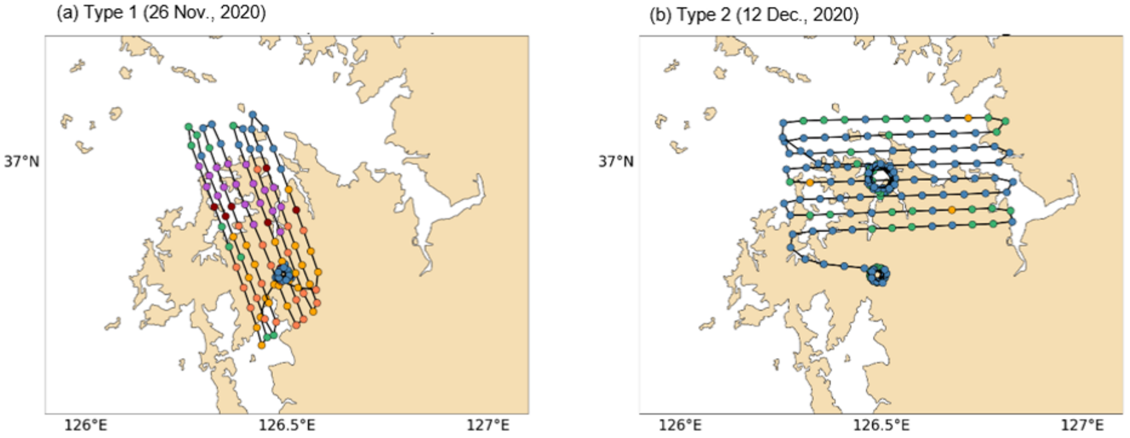

Figure 2. Flight tracks for two Cessna Grand Caravan 208 B aircraft over Pandora sites (left) PA_4 and (right) PA_1 during the GMAP-2020 campaign. Colored circles indicate airborne NO_2 concentration observations. Stacked circles indicate spiral flights conducted over two sites.

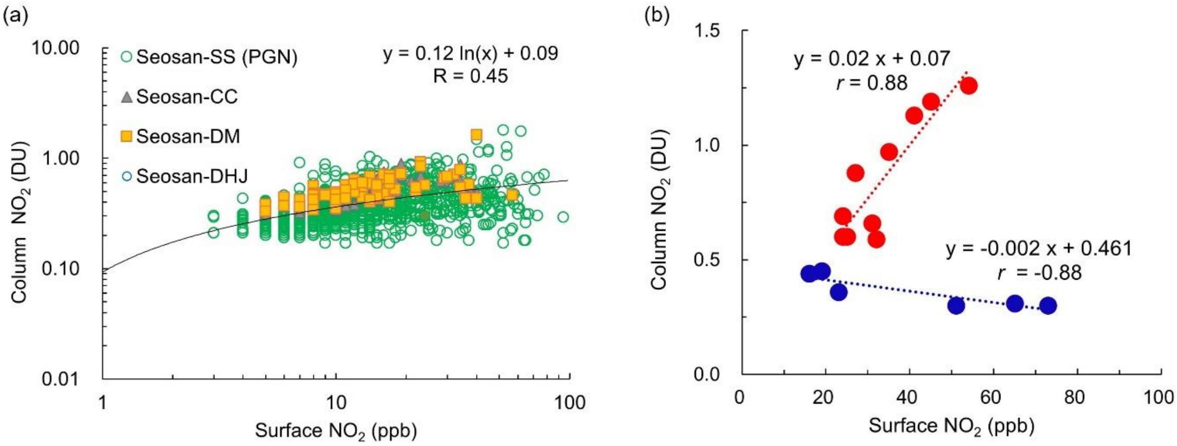

Figure 3. a) Pandora column (PC) NO_2 measurements as a function of surface *in situ* (SI) NO_2 observations at Pandora sites PA_1–PA_3 during the GMAP-2020 campaign and PA_4 during a 1-year period. A logarithmic regression model was used to evaluate the relationship between PC and SI measurements (black line). (b) Sample scatterplots of PC-NO_2 and SI-NO_2 for February 24 (red) and April 21 (blue), 2021.

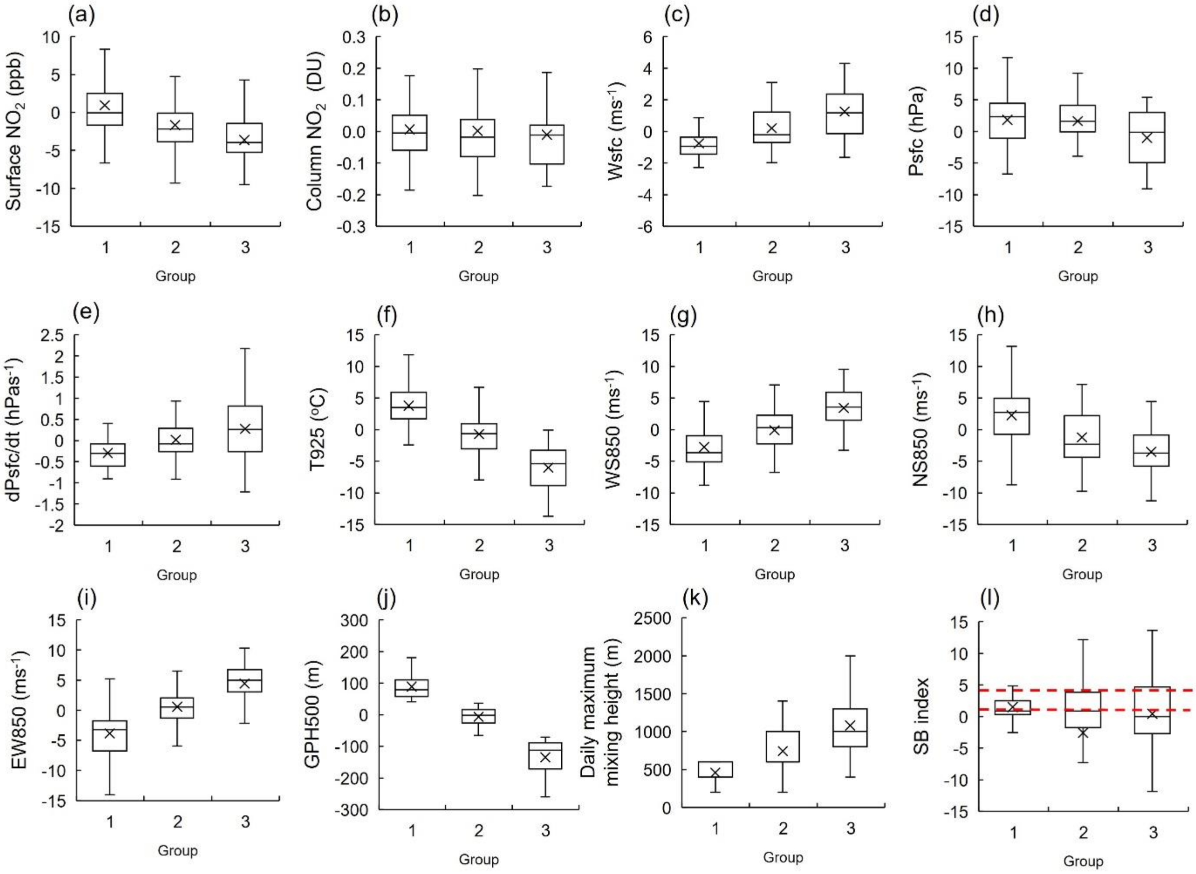

Figure 4. K-means clustering yielded three groups of cases for (a) surface NO$_2$ and (b) PC-NO$_2$, associated with eight meteorological variables: (c) surface wind speed (Wsfc), (d) Psfc, (e) Psfc tendency (dPsfc/dt), (f) 925-hPa air temperature (T925), (g) 850-hPa wind speed (W850), (h) 850-hPa north–south wind component (NS850), (i) 850-hPa east–west wind component (EW850), and (j) 500-hPa geopotential height (GPH500). All data were de-seasonalized using the 30-day moving average, except PC-NO$_2$, for which the monthly average was used. (k) Simulated daily maximum mixing height (not directly clustered). (l) Box and whisker plots of the sea breeze index (SBI) at Seosan for the 1-year period. Red dots indicate the critical SBI (a value of 3), suggested by Biggs and Graves (1962).

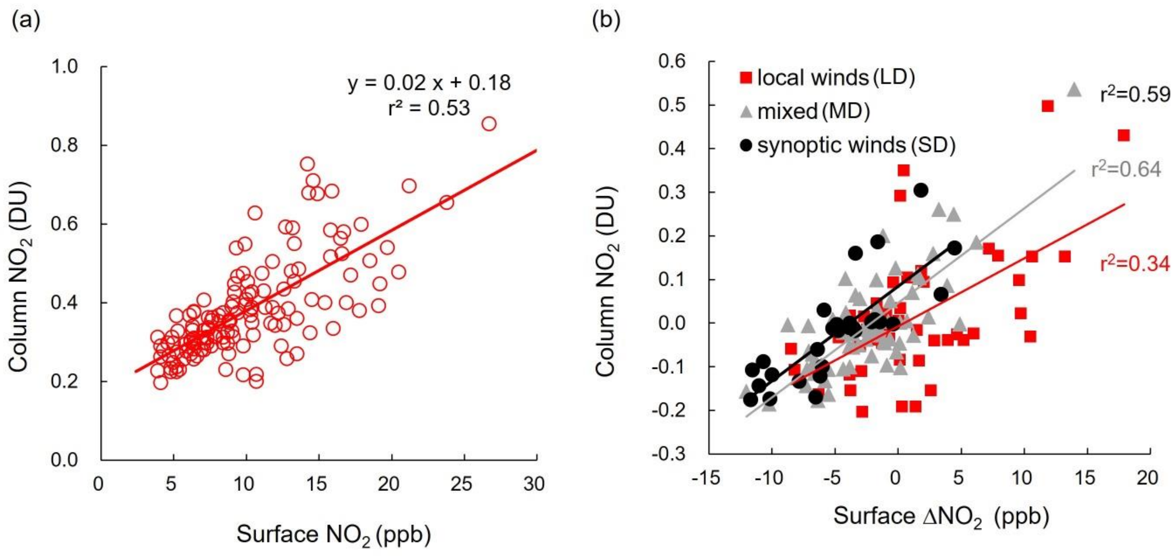

Figure 5. (a) Scatterplots of daytime measurements at site PA$_4$ (a) PC-NO$_2$ vs. SI-NO$_2$ under all meteorological conditions and (b) PC-NO$_2$ vs. Surface △NO$_2$ in each meteorological condition over a 1-year period (November 12, 2020–October 30, 2021). Here Surface △NO$_2$ = SI-NO$_2$ – (30-day moving average) SI-NO$_2$.

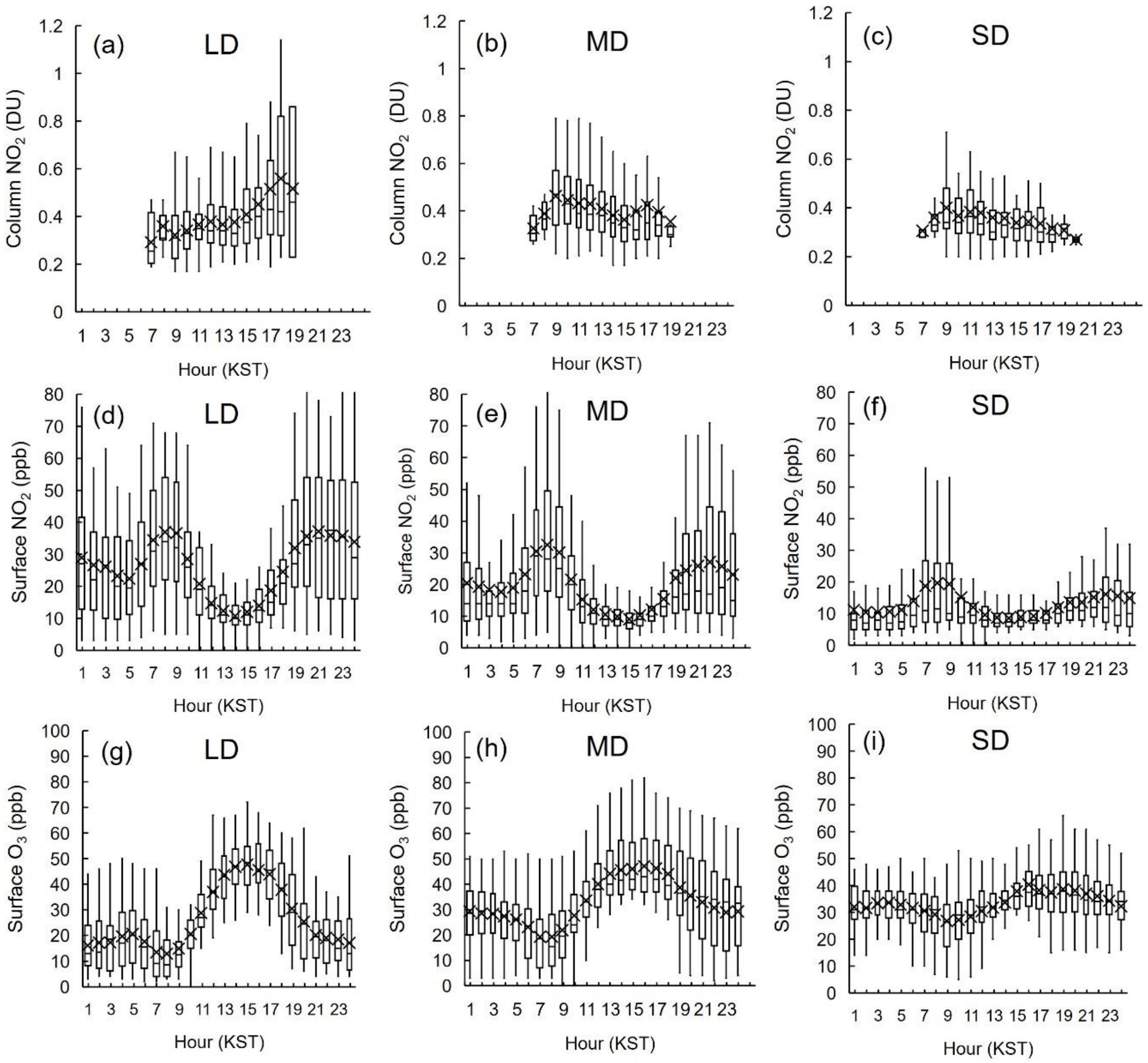

Figure 6. Box and whisker plots of diurnal variation in (a–c) PC-NO_2, (d–f) SI-NO_2, and (g–i) surface O_3 under synoptic wind-dominant (SD), mixed (MD), and local wind-dominant (LD) conditions in Seosan during a 1-year period (November 12, 2020–October 30, 2021).

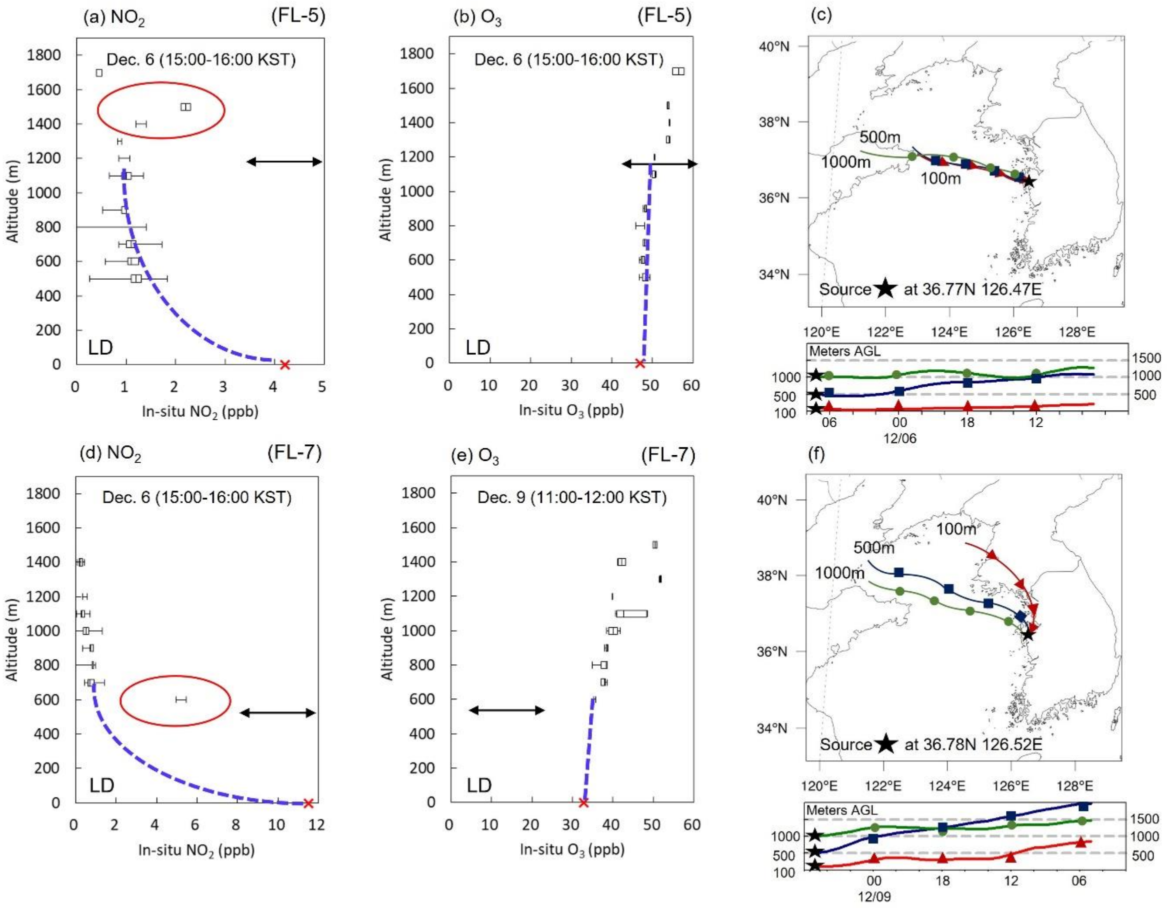

Figure 7. Box and whisker plots of the vertical NO$_2$ and O$_3$ profiles measured by GMAP aircraft superposed with *in situ* AQMS$_1$ measurements during flights (a, b) FL-5 (December 6) and (d, e) FL-7 (December 6 and 9). Blue dashed lines are linear regression lines fitted to NO$_2$ and O$_3$ profiles within the planetary boundary layer (PBL). Black arrows indicate the simulated PBL height (PBLH) obtained from the Korea Meteorological Administration (KMA). HSYPLIT 24-h backward trajectories in Seosan are shown at altitudes of 100, 500, and 1,000 m, starting at 1600 KST on November 26 and 1200 KST on December 12.

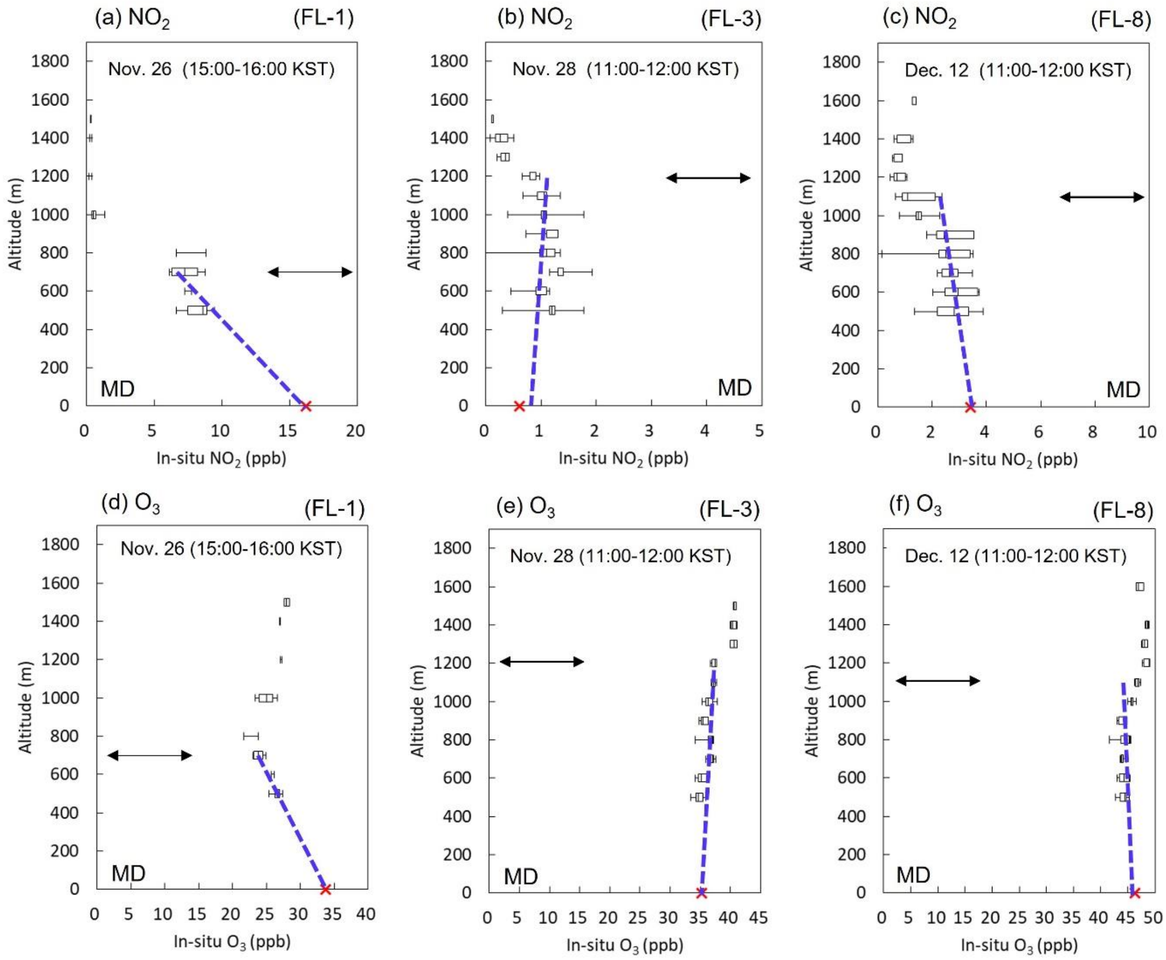

Figure 8. Box and whisker plots of vertical profiles obtained from GMAP aircraft superposed with *in situ* AQMS measurements for (1) NO_2 and (2) O_3 for flights (a) FL-1 (November 26), (b) FL-3 (November 28), and (c) FL-8 (December 12). Blue dashed lines are linear regression lines fitted to NO_2 and O_3 in the PBL. Black arrows indicate PBLH simulated by the Hybrid Single-Particle Lagrangian Integrated Trajectory (HYSPLIT) Global Forecast System (GFS).

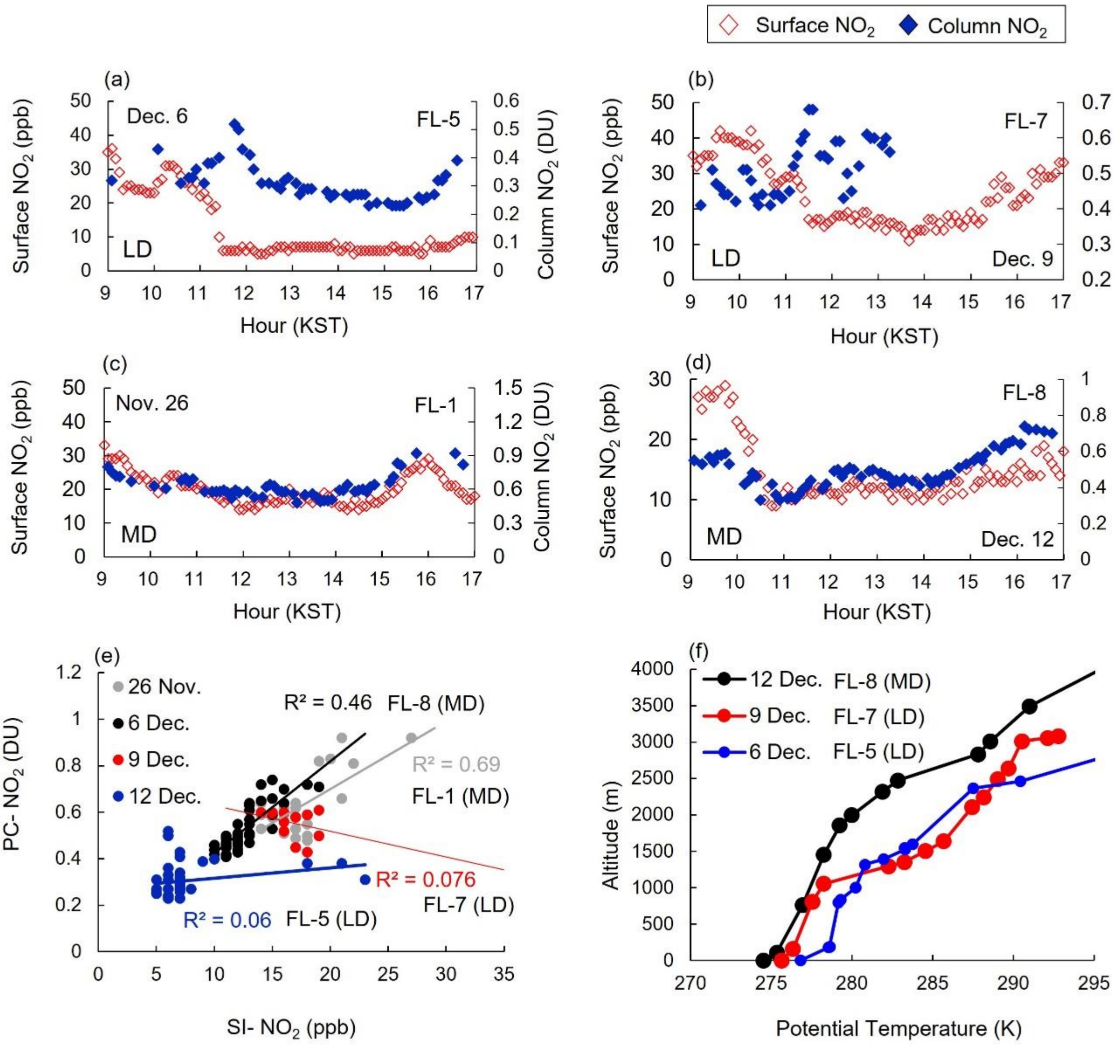

Figure 9. Time series and scatterplots of PC-NO$_2$ and SI-NO$_2$ at PA$_2$ on (a) December 6, (b) December 9, (c) November 26, and (d) December 12. (e) Scatterplot of PC-NO$_2$ and SI-NO$_2$ on December 6 (blue), December 9 (red), November 26 (gray), and December 12 (black). (f) Vertical potential temperature profiles on December 6, 9, and 12, 2020. Radiosonde data for November 26, 2020 are missing.

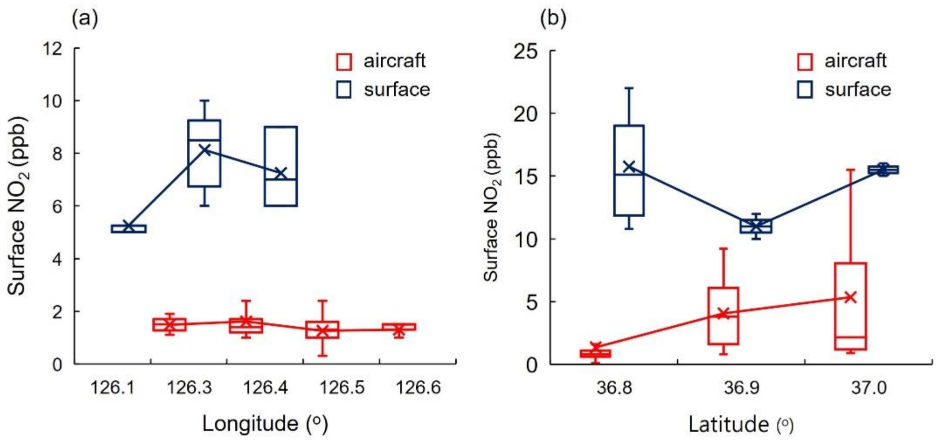

Figure 10. Latitudinal NO_2 distribution at the surface and 600 m over PA_4 (Seosan Super Site), averaged during (a) 1300–1600 KST on December 6 (FL-5) by longitude and (b) 1200–1400 KST on December 9 (FL-7) by latitude, obtained from airborne (blue) and surface measurements (red).

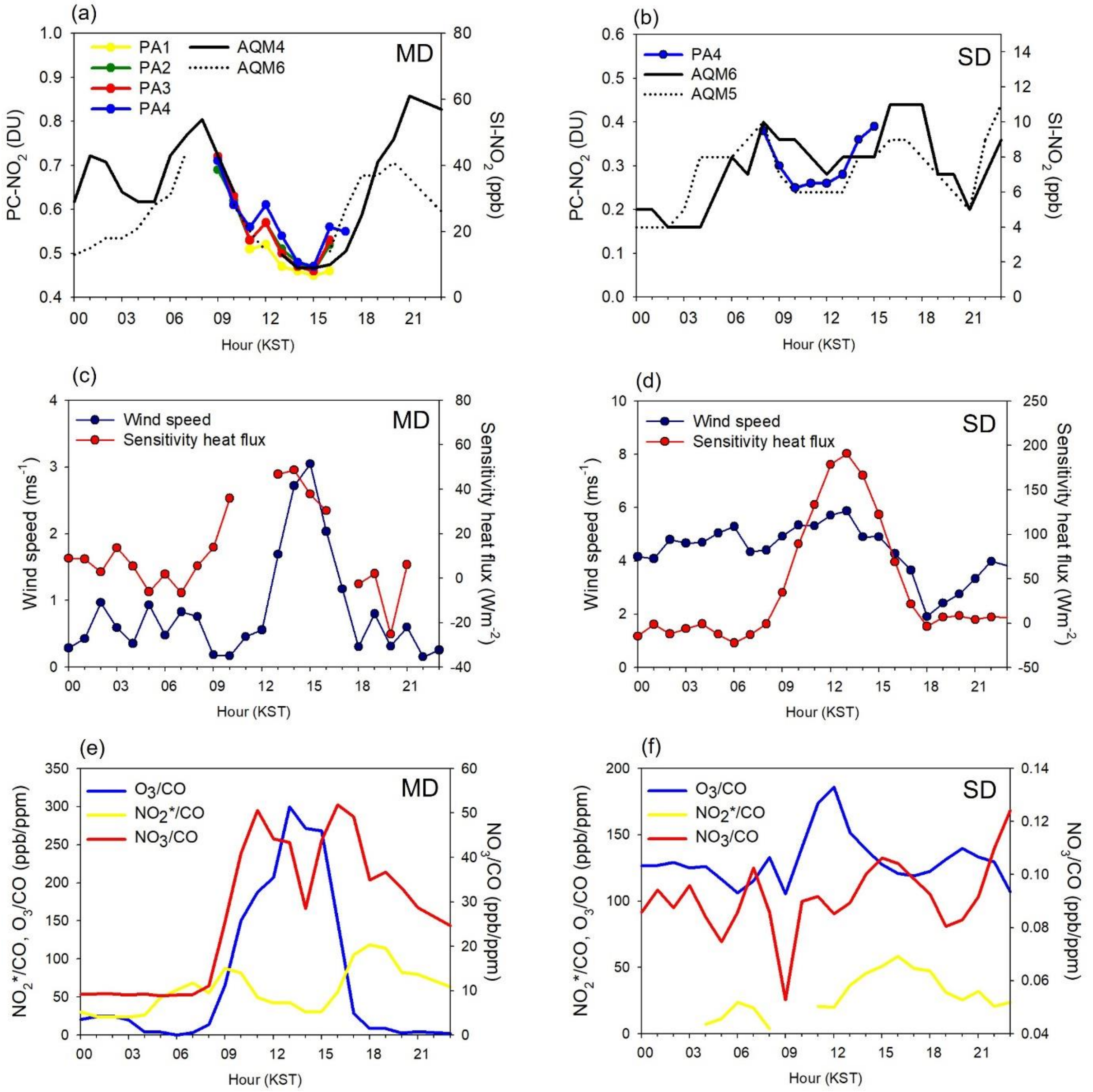

Figure 11. Examples of the diurnal variation on November 25 (a, c, e) and December 14 (b, d, f). (a, b) Column NO$_2$ at sites PA$_1$–PA$_4$ and surface NO$_2$ at air quality monitoring sites AQM$_4$ and AQM$_6$. (c, d) Sensible heat fluxes and surface wind speed at PA$_4$. (e, f) Diurnal variation in NO$_2$, NO$_2^-$, and O$_3$ normalized by CO. Figure 1 shows the locations of the measurement sites.